Sneha, M., Lewis-Borrell, L., Shchepanovska, D., Bhattacherjee, A., Tyler, J. L., & Orr-Ewing, A. J. (2020). Solvent-dependent photochemical dynamics of a phenoxazine-based photoredox catalyst. *Zeitschrift für Physikalische Chemie*, *234*, 1475 - 1494. https://doi.org/10.1515/zpch-2020-1624

Solvent-dependent photochemical dynamics of a phenoxazine-based photoredox catalyst

Mahima Sneha*, Luke Lewis-Borrell, Darya Shchepanovska, Aditi Bhattacherjee,[(a)] Jasper Tyler and Andrew J. Orr-Ewing*

School of Chemistry, University of Bristol, Cantock's Close, Bristol BS8 1TS, UK

[(a)] *Current address: AMOLF, Science Park 104, 1098 XG Amsterdam, The Netherlands*

* Authors for correspondence: mahima.sneha@bristol.ac.uk; a.orr-ewing@bristol.ac.uk

ORCID: Mahima Sneha 0000-0003-4896-6915; Luke Lewis-Borrell 0000-0002-6198-722X; Darya Shchepanovska 0000-0002-2676-8152; Aditi Bhattacherjee 0000-0001-7146-1128; Jasper Tyler 0000-0002-3155-1847; Andrew J. Orr-Ewing 0000-0001-5551-9609.

Keywords: photochemistry; transient absorption spectroscopy; ultrafast dynamics; organic photocatalyst.

Running title: Photo-induced phenoxazine dynamics

Abstract

Organic substitutes for ruthenium and iridium complexes are increasingly finding applications in chemical syntheses involving photoredox catalysis. However, the performance of these organic compounds as electron-transfer photocatalysts depends on their accessible photochemical pathways and excited state lifetimes. Here, the UV-induced dynamics of N-phenyl phenoxazine, chosen as a prototypical N-aryl phenoxazine organic photoredox catalyst, are explored in three solvents, N,N-dimethyl formamide, dichloromethane and toluene, using ultrafast transient absorption spectroscopy. Quantum chemistry calculations reveal the locally excited or charge-transfer electronic character of the excited states, and are used to assign the transient electronic and vibrational bands observed. In toluene-d_8, complete ground-state recovery is (31 ± 3) % by internal conversion (IC) from the photo-excited state (or from S_1 after IC but before complete vibrational relaxation), (13 ± 2) % via direct decay from vibrationally relaxed S_1 (most likely radiative decay, with an estimated radiative lifetime of 13 ns) and (56 ± 3) % via the T_1 state (with intersystem crossing (ISC) rate coefficient $k_{ISC} = (3.3 \pm 0.2) \times 10^8$ s^{-1}). In dichloromethane, we find evidence for excited state N-phenyl phenoxazine reaction with the solvent. Excited state lifetimes, ISC rates, and ground-state recovery show only modest variation with changes to the solvent environment because of the locally excited character of the S_1 and T_1 states.

Introduction

The rapid emergence of photoredox catalysis in chemical and materials synthesis reflects the wide range of chemical transformations that can be driven selectively and controllably this way using visible or near ultraviolet (UV) light sources. Initial applications made use of ruthenium and iridium complexes such as $Ru(bpy)_3^{2+}$ and $Ir(ppy)_3$ because of their favourable excited-state properties and redox potentials for single-electron transfer (SET) reactions.[1] Although these well-characterized and tested metal complexes remain in widespread use, efforts are underway to find more sustainable replacements. Alternative strategies include replacing the Ru^{2+} or Ir^{3+} complexes with those of an Earth-abundant metal such as Nickel,[2, 3] or switching to the use of organic dyes.[4] Here, the focus will be on this latter approach.

For an organic dye to be an effective organic photoredox catalyst (OPC), it should meet certain desirable criteria. For example, it should strongly absorb near-UV or visible light and possess first-excited singlet (S_1) or triplet (T_1) states with lifetimes long enough for diffusive SET reactions. Moreover, these excited states should have redox potentials relative to the $OPC^{\cdot+}$ or $OPC^{\cdot-}$ radical cation or anion that are sufficient to initiate the catalysed chemical reaction by SET. Numerous candidate OPCs have been proposed, characterized and tested, with progress up to 2016 summarized in the extensive review by Romero and Nicewicz.[4] More recently, classes of OPCs based on N,N-diaryl dihydrophenazines, N-aryl phenoxazines, and N-aryl phenothiazines have been applied as photoredox catalysts for controlled atom-transfer radical polymerization (ATRP).[5-10] For these OPC classes, structural design principles have been developed based on both the observation of as-grown polymer properties[11-13] and transient absorption spectroscopy studies of excited-state lifetimes and SET rates.[14-17] Transient absorption spectroscopy has also been applied to other examples of photoredox reactions and over timescales spanning sub-picosecond to millisecond to explore multi-step reaction mechanisms.[15, 18-21]

The complex photochemistry of these OPCs depends sensitively on the molecular architecture and the choice of solvent. For example, the ordering of excited states, de-activation pathways to the ground state, rates of intersystem crossing (ISC), triplet-state quantum yields, and rates of bimolecular SET reactions can all be modified by changes to the excited-state electronic character[22, 23] and by different solute-solvent interactions.[24, 25] N-aryl groups pendant to dihydrophenazine, phenoxazine and phenothiazine cores and derivatized with electron withdrawing or donating groups can stabilize S_1 and T_1 states with greater charge-transfer (CT) or local excitation (LE) character respectively, and the ordering of excited states with these characters also depends on the solvent polarity. Arguments have been presented that T_1 CT character enhances the efficacy of OPCs used for ATRP,[11-13] and trends in measured rates of dissociative SET have also been discussed in the context of Marcus-Savéant theory.[14]

Because the excited state photodynamics of OPCs depend sensitively on their molecular structures, benchmarking experimental and computational studies are required for model systems from which

variations caused by structural modifications can be interpreted. Here, we examine the ultrafast photochemistry of one such model photocatalyst, N-phenyl phenoxazine (referred to here as NPP). This compound is chosen as the simplest example of the numerous N-aryl phenoxazines derivatives currently being tested as candidate OPCs and tailored to have desirable absorption spectra and excited state reduction potentials.[12] The properties of the excited states of NPP are examined using a combination of transient vibrational absorption spectroscopy (TVAS) and transient electronic absorption spectroscopy (TEAS) measurements using infrared (IR) and UV/visible probe wavelengths respectively. Experiments conducted in N,N-dimethyl formamide (DMF), dichloromethane (DCM) and toluene explore the effects of solvent on the photodynamics. Interpretation of the experimental observations draws upon quantum chemical calculations of the properties of the excited electronic states of NPP.

Experimental

Transient absorption spectroscopy measurements were made using an ultrafast laser system at the University of Bristol (UoB) and the LIFEtime facility at the STFC Rutherford Appleton Laboratory. Both set-ups have been described elsewhere,[26-29] and only brief accounts of key experimental procedures are provided here. In all the reported experiments, 3.2 mM solutions of NPP were photoexcited at a UV wavelength of λ_{exc} = 318 nm using laser pulses of duration ~50 fs (UoB laboratory) or <260 fs (LIFEtime) with maximum energies of 150 nJ pulse^{-1} to minimize the risk of multiphoton processes. A peristaltic pump continuously circulated the NPP solutions through a Harrick cell with a pair of CaF_2 windows separated by Teflon spacers chosen to give a pathlength of 380 μm (for TEAS) or 100 μm (for TVAS). With this combination of concentration and pathlength, the sample absorbance at 318 nm was below 0.5 for TVAS. NPP was synthesized according to the procedure described in Ref. [8] and its purity was confirmed by NMR prior to use. Further details are provided in Supporting Information. For transient spectroscopy experiments, solvents were either spectroscopic grade (Toluene, 99.8%) or anhydrous (dichloromethane (DCM) and N,N-dimethylformamide (DMF), Sigma Aldrich 99.8%). For TVAS measurements, toluene-d_8 (Sigma Aldrich, 99.6 atom% D) was used in place of toluene to avoid interfering solvent absorption bands. Nitrogen was bubbled through all sample solutions immediately prior to use to displace dissolved O_2.

Pulses of broadband IR or UV/visible radiation probed the sample solutions by TVAS and TEAS respectively at selected time delays after the 318-nm excitation pulse. TEAS measurements at UoB spanned delay times up to 1.3 ns with an instrument response function (IRF) of ~120 fs after chirp correction,[26] whereas TVAS measurements with LIFEtime extended beyond 1000 ns with an IRF of ~200 fs.[18, 28, 29] The TEAS probe pulses were produced by white-light continuum (WLC) generation in a flat CaF_2 optic using a gently focused portion of the 800-nm fundamental output from a Ti:sapphire regenerative amplifier (Coherent Legend Elite HE+, 5 W, 1 kHz repetition rate; seeded by a Coherent Vitara-S oscillator). The resulting WLC spanned the wavelength range from 350 – 700 nm and was spatially overlapped with the pump 318-nm pulses at the centre of the sample cell. After transmission

through the sample, the probe pulses were dispersed in a calibrated spectrograph (Andor, Shamrock 163) fitted with a 1024-element photodiode array (Entwicklungsbüro Stresing) for acquisition of wavelength-resolved absorbance changes induced by the UV pump pulses. Mid-IR probe pulses for TVAS were produced by difference frequency generation in GaSe of the outputs from a pair of optical parametric amplifiers (OPAs, Light Conversion Orpheus ONE) synchronously pumped at 1030 nm by a 100 kHz, 6 W Yb:KGW laser system (Light Conversion Pharos SP). The two OPAs provided independently tuneable wavenumber coverage over spectral bandwidths of ~200 cm^{-1}. Both IR probe pulses were spatially overlapped with the UV pump pulse at the sample, and were separately dispersed onto cryogenically cooled 128-element Mercury-Cadmium-Telluride (MCT) arrays (Infrared Associates Inc.). The detected signals were integrated and digitized by FPAS systems (Infrared Systems Development Corp FPAS 0144). TVAS time delays up to 12 ns were controlled by a multi-pass mechanical delay stage, with longer time delays selected using pulse-picking electronics. In all TEAS and TVAS measurements, the polarizations of the pump and probe laser pulses were set at magic angle (54.7°) to remove any effects of rotational anisotropy on the measured time-evolving signals.

Extensive averaging during the acquisition of experimental spectra ensured satisfactory signal-to-noise ratios. Transient absorption spectra were processed without the use of shot-to-shot division by reference spectra of the probe laser pulses because of the stability of the laser systems. The averaged spectra obtained at multiple pump-probe time delays were analysed by spectral decomposition using the KOALA software package[30] to extract the time-evolutions of the component excited-state absorption (ESA), stimulated emission (SE) and ground-state bleach (GSB) features. Further fitting to user-defined kinetic functions was performed in Origin software (OriginLab, Origin 2018b). More specific details of these analyses are provided in the Results and Discussion section.

Calculations

Geometry optimisation of NPP and vibrational frequency calculations in toluene, DCM and DMF solvents were performed using the Gaussian 09 program.[31] The CAM-B3LYP density functional was used with a 6-31+G* basis and Grimme dispersion corrections with Becke-Johnson damping. Solute-solvent interaction effects were accounted for by the conductor polarizable continuum model (CPCM). TDDFT optimisations of S_1 and T_1 geometries were also performed in toluene and DMF, with normal mode analysis confirming that these geometries were the minima on their respective potential energy surfaces. An anharmonicity scaling factor of 0.953 was applied to the calculated normal mode frequencies prior to comparisons with experimental spectra.[32]

Vertical excitation energies and oscillator strengths were calculated using the ORCA program (v4.2.0)[33] at the TDDFT/CAM-B3LYP/6-31+G* level of theory. The solvent shift was computed via the SMD solvation model that includes both electrostatic and non-electrostatic contributions. Transition dipole moments and oscillator strengths between excited states for the S_1 and T_1 geometries were computed

from the results of the TDDFT calculations using the Multiwfn program for electronic wavefunction analysis.[34] These computational results are reported in Tables S1 – S9 of Supporting Information.

Results and Discussion

The structure of NPP and its measured absorption spectrum in toluene are shown in **Figure 1**, together with computed maps of the changes in electron density associated with excitations from S_0 to the first three singlet excited states. The corresponding plots of electron density changes for NPP in DMF and DCM are shown in Figure S10 of the Supporting Information. In the S_0 state, the phenyl ring orients preferentially perpendicular to the plane of the phenoxazine core to reduce steric crowding.

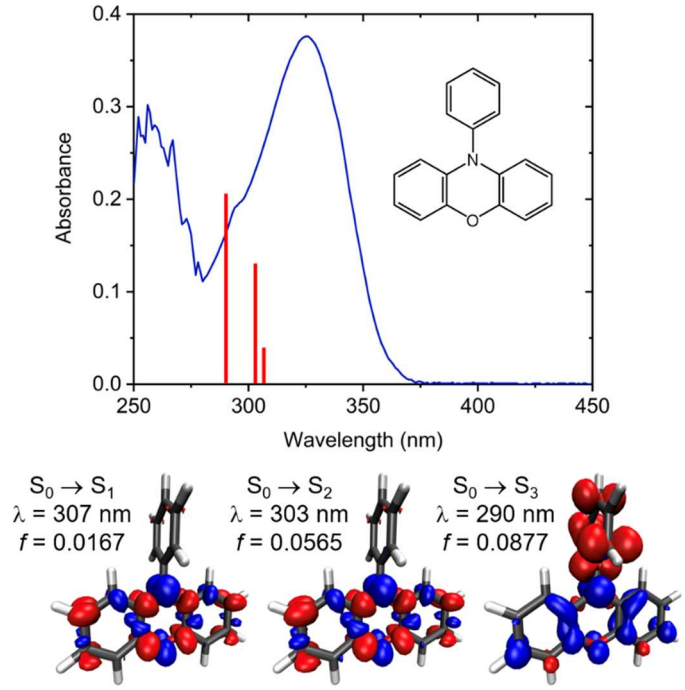

Figure 1: Top: UV absorption spectrum of a 3.2 mM solution of NPP in toluene (sample pathlength = 100 μm). The structure of NPP is shown as an inset. Similar absorption spectra were obtained in DCM and DMF (Supporting Information Figure S1). Bottom: Electron density difference plots between the S_0 and S_n states for n = 1, 2 and 3 at the S_0 geometry, showing the local excitation character for $S_0 \rightarrow S_1$ and $S_0 \rightarrow S_2$ transitions, and greater charger transfer character for the S_3 state. The calculations were performed in toluene, the densities are visualised with isovalues set to 0.002, and an increase in electron density is shown in red, with a decrease in blue. Predicted excitation wavelengths (λ) and oscillator strengths (*f*) are given for the three transitions. These computed properties are also shown as red vertical bars superimposed on the absorption spectrum, with the bar heights proportional to *f* values.

Absorption spectra in the 250 – 450 nm range are compared in Figure S1 of Supporting Information for NPP solutions in toluene, DCM and DMF. The band centred near 325 nm shows only modest (≤ 2 nm) shifts in its wavelength of maximum absorption in the three solvents. According to our calculations for NPP in toluene, the longest wavelength absorption (computed to arise at λ = 307 nm) corresponds to the weak $S_0 \rightarrow S_1$ transition, with oscillator strength $f = 0.017$. The change in electron density (**Figure 1**) indicates predominantly LE character on the core of the phenoxazine, with negligible CT character corresponding to electron density shifting from the core to the N-phenyl group. At slightly higher energy (λ = 303 nm in toluene), the stronger $S_0 \rightarrow S_2$ $\pi \rightarrow \pi^*$ absorption band with $f \sim 0.056$ has similar LE character, but the $S_0 \rightarrow S_3$ transition (λ = 290 nm, $f = 0.0877$ in toluene) shows greater CT character. Similar calculations in DCM and DMF (Figure S10) predict $S_0 \rightarrow S_1$, S_2 and S_3 transitions at λ = 307, 294 and 289 (DCM) or 287 nm (DMF) respectively, with oscillator strengths of $f = 0.022$, 0.029 and 0.128 in DMF. The corresponding f values for DCM are 0.028, 0.039 and 0.115. The S_2 state now shows CT character and has been stabilized relative to the LE states by the more polar DCM or DMF solvent. At our chosen centre excitation wavelength of 318 nm (with an ~ 3 nm bandwidth), the likelihood is therefore that we are exciting a mixture of states, with the LE S_2 and CT S_3 state for NPP in toluene, and the LE S_3 state in DCM or DMF, the main contributors. We refer hereafter to UV excitation to S_n with $n = 2$ or 3 depending on the solvent, but we recognize there may also be some weaker direct excitation of S_1 in our experiments. Fluorescence spectra for NPP solutions are also shown in Figure S1 of Supporting Information. The emission bands peak at wavelengths around 400 nm for all three solvents, consistent with the emitting S_1 state having little or no CT character.

Transient electronic absorption spectra of NPP solutions in DMF, DCM and toluene are compared in **Figure 2**. The drop in differential absorption approaching 350 nm is a consequence of the combined effects of the spectrum of the WLC used as a probe, which decays in intensity in this region, and the onset of an NPP ground-state absorption band. The dips observed around 636 nm correspond to pump laser light scattered by the sample and detected after second-order diffraction from the spectrometer grating. The TEA spectra feature a prominent band with Gaussian profile centred near 460 nm in all three solvents. This feature grows at the later time delays displayed and is accordingly assigned to absorption from the T_1 state of NPP. This assignment is supported by calculations reported in the Supporting Information which predict a strong T_1 absorption band (with oscillator strength $f = 0.13$) at 513 nm in DMF and 496 nm in toluene (with $f = 0.08$). Similar triplet state ESA bands were observed by Sartor *et al*. for modified versions of NPP with phenyl or biphenyl core substituents, albeit shifted to longer wavelength by the additional core conjugation.[13, 16] At shorter time delays, the TEA spectra show solvent-dependent evolutions, with loss of absorption at wavelengths above 550 nm and growth then decay of an intermediate band peaking near 520 nm (with a secondary peak at wavelengths around 390 nm). This double-peaked feature is more prominent for spectra measured in DCM or DMF than in toluene where it is barely discernible as a broad feature above 500 nm. Plausible assignments of the

rapidly decaying long-wavelength absorption and the 520-nm intermediate band are to ESA from the initially photoexcited S_n (n = 2 or 3) state and the S_1 state into which it relaxes by internal conversion (IC). Our calculations summarized in the Supporting Information predict a strong S_1 absorption band at 560 nm in DMF (f = 0.44) and 565 nm in toluene (f = 0.14). The lower oscillator strength in toluene may explain why this feature is less distinct for TEA spectra measured in this solvent. Decay of the S_1 state population is either by ISC, resulting in growth of T_1 ESA, relaxation by IC or fluorescence to S_0, or reaction with the solvent for which evidence is presented below in the case of DCM. There is no clear evidence for a stimulated emission band, most likely because the ESA-band oscillator strengths are more than 5× larger than for the $S_1 \rightarrow S_0$ emission.

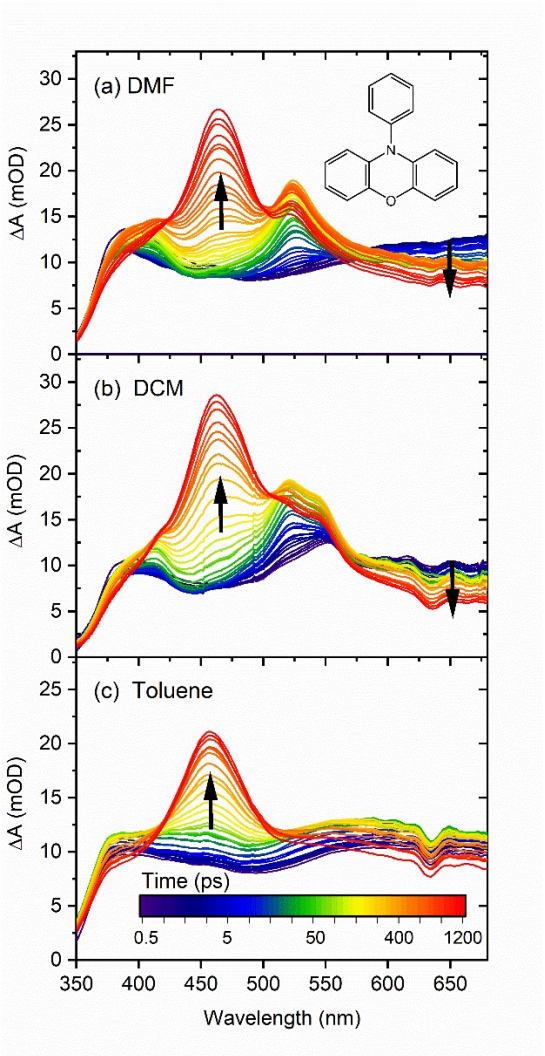

Figure 2: Transient electronic absorption spectra obtained for the 318-nm photoexcitation of NPP in three organic solvents: (a) DMF; (b) DCM; (c) toluene. The colours represent spectra obtained at different time delays after the photoexcitation, as shown by the inset key in the bottom panel. Black arrows show the directions of change of selected features with time. The spectral features are

discussed in the main text. The dips centred at 636 nm result from pump-laser scatter detected in second order by the spectrometer.

Spectral decomposition in the KOALA program resulted in time-dependent integrated band intensities for the three solutions, examples of which are plotted in **Figure 3**. This decomposition requires choices to be made for the basis functions corresponding to S_n, S_1 and T_1 ESA bands. We fitted the T_1 ESA band to a Gaussian function of fixed central wavelength and width, and for measurements in DMF we used a double-peaked basis function with maxima at 520 nm and 390 nm to model the double-peaked S_1 ESA. This function corresponded to a mid-time spectrum measured at ~20 ps. The remaining broad absorption spanning 350 – 680 nm (the range covered by the combination of WLC and spectrometer) is assigned to S_n ESA and was modelled using an early time spectrum (typically at a time delay of 600 fs, before significant growth of S_1 and T_1 population) as a basis function. These basis function choices, the modified procedures used for analysis of measurements in toluene and DCM, and examples of decomposition of TEA spectra in all three solvents are shown in Figures S3 – S8 of the Supporting Information.

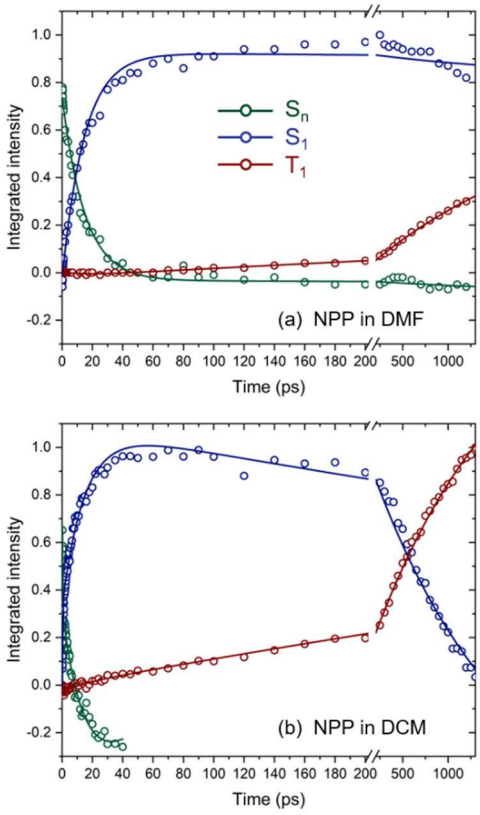

Figure 3: Examples of excited state population kinetics obtained from analysis of the TEAS data shown in Figure 2 for the 318-nm photoexcitation of NPP in: (a) DMF; (b) DCM. Integrated band intensities for the excited states are represented by coloured circles for S_n (green), S_1 (blue) and T_1 (red). Solid lines are global fits to bi- or tri-exponential functions for each sample. Negative going

integrated band intensities for the S_n components indicate an offset caused by baseline effects in the basis function used for spectral decomposition but do not affect the analysis. Note the axis break and change of scale for time delays beyond 200 ps. Measurements in DCM also show evidence of $NPP^{\cdot+}$ formation by electron transfer with the solvent (see Figures S7 and S8 of Supporting Information). The corresponding kinetic data for NPP in toluene solutions are not shown because of the difficulty of accurately separating S_n and S_1 ESA features in the transient absorption spectra obtained in this solvent.

The time-dependent integrated band intensities for excited-state absorption features in the TEA spectra are consistent with a sequential kinetic model in which the photoexcited S_n state populates S_1 by IC, and this S_1 population in turn decays by ISC (populating T_1 either directly, or indirectly via higher T_n states) and non-radiative or radiative relaxation to S_0. The time constants obtained from kinetic fits to the TEAS data are summarized in **Table 1**. These fits to bi- or tri-exponential functions treated a data set of the type shown in Figure 3(a) or (b) globally by constraining shared time constants for decay of population of one state and growth of another to be equal in simultaneous fits. The choice of bi- or -tri-exponential fit functions was made by examination of systematic contributions to the fit residuals. Where amplitudes of fit components were negligible, the time constants are not reported in **Table 1**. For example, the rise in intensity of the T_1 band was dominated by an exponential function with ~ 2 ns time constant, with no meaningful contribution from faster exponential rise terms. Error ranges in the reported time constants in **Table 1** derive from the fitting uncertainties and do not reflect possible systematic errors deriving from our choice of basis functions used for spectral decomposition. The >1 ns time constants (τ_3) for population decay in the S_1 state and growth in the T_1 state were poorly defined by TEAS measurements limited to maximum time delays of 1.3 ns. Hence, values for τ_3 established from TVAS experiments discussed below and extending to longer time delays were used as fixed parameters in the fits. These τ_3 values were confirmed as corresponding to S_1 state lifetimes by time-correlated single photon counting (TCSPC) fluorescence emission measurements made for NPP solutions in DMF, DCM and toluene. The TCSPC measurements obtained exponential time constants for decay of NPP fluorescence intensity of 2.60 ± 0.02 ns (DMF), 1.20 ± 0.01 ns (DCM) and 2.75 ± 0.01 ns (toluene).

The TEAS data do not reveal the origins of the two time constants (τ_1 and τ_2) for decay of S_n and growth of S_1 population derived from measurements in DCM (**Table 1**), for which several explanations are possible. These two components of relaxation may originate from bifurcating dynamical pathways in the S_n state,[35] changing contributions to the transient absorption spectra resulting from the $S_n \rightarrow S_1$ IC step and subsequent vibrational cooling in the S_1 state, or initial photoexcitation of more than one electronically excited state.

Table 1: Time constants obtained from bi- or tri-exponential analysis of the evolution of the intensities of bands observed by transient electronic absorption spectroscopy and assigned to the S_n, S_1 and T_1 states of NPP. The global fitting of kinetic data for all electronic states gives matching entries in more than one column for a given solvent. A dash indicates the time constant was not required in, or extracted from, the multi-exponential fitting.

	S_n (n =2 or 3)		S_1			T_1
Solvent	τ_1 / ps (decay)	τ_2 / ps (decay)	τ_1 / ps (growth)	τ_2 / ps (growth)	τ_3 / ns [(a)] (decay)	τ_3 / ns [(a)] (growth)
DMF	–	14.8 ± 0.3	–	14.8 ± 0.3	2.1 ± 0.1	2.1 ± 0.1
DCM	0.3 ± 0.1	14.8 ± 0.4	0.3 ± 0.1	14.8 ± 0.4	1.5 ± 0.2	1.5 ± 0.2
Toluene	–	–	–	22.8 ± 1.0	2.4 ± 0.2	2.4 ± 0.2

(a) The long-time decay of S_1 and growth of T_1 populations extend beyond the longest times accessible to the TEAS measurements. The associated time constants in the marked columns are therefore values from analysis of TVAS measurements (see below) and were fixed (without the associated uncertainty) in the fits to TEAS data.

The interpretation of the TEA spectra is supported by the TVAS data, examples of which are presented in **Figure 4** for the probe wavenumber range from 1475 – 1650 cm^{-1}. Measurements in toluene used toluene-d_8 to minimize interference by solvent bands in the probe wavenumber region, although a remaining strong solvent band prevents analysis of the spectra in the region from 1560 – 1590 cm^{-1}. In DMF, solvent absorption bands limited the observation window to 1530 – 1610 cm^{-1}. Bands corresponding to ground-state NPP are evident as negative-going GSB features because of ground-state population depletion by the excitation laser pulse at 318 nm. These assignments to NPP are supported by steady state FTIR spectra of NPP solutions, as shown in Figure S2 of the Supporting Information. Computed (and anharmonically corrected) vibrational frequencies (in cm^{-1}) are reported in **Table 2** for NPP S_0, S_1 and T_1 states in DMF and in toluene solutions, and are compared to experimentally observed bands where possible. A broad transient absorption feature spanning 1500 – 1590 cm^{-1} is assigned to ESA from the S_1 state because of its observed wavenumber range and time-dependence. The reason for the breadth of the band is not apparent from the calculations which predict a single strong feature and other much weaker bands in this wavenumber region. We see no bands that can be assigned to NPP (T_1) ESA in the spectral region probed for reasons that become apparent by reference to the calculations: the predicted T_1 band positions are masked by strong solvent absorptions in DMF, and the bands are computed to be weak in all three solvents. Kinetic analyses of the integrated intensities obtained by band fitting of TVAS data are shown in Figure S9 of Supporting Information.

Table 2: Computed IR band wavenumbers (scaled by an anharmonic correction factor of 0.953 – see main text) and intensities for the S_0, S_1 and T_1 states of NPP in DMF, toluene and DCM solutions. The table lists the strong IR bands computed to appear in the spectral window probed here by TVAS. Experimentally observed values are given in parentheses and labelled as GSB or ESA features.

	DMF		Toluene		DCM	
NPP state	$\bar{\nu}$ / cm^{-1}	Intensity / km mol^{-1}	$\bar{\nu}$ / cm^{-1}	Intensity / km mol^{-1}	$\bar{\nu}$ / cm^{-1}	Intensity / km mol^{-1}
S_0	1596 (1594 GSB)	67	1483 (1491 GSB)	911	1478 (1491 GSB)	1072
S_1	1576 (1525 - 1590 ESA)	111	1580 (1500 - 1590 ESA)	100	1483 1576 (1500 – 1590 ESA)	229 116
T_1	1486 1485	46 30	1459 1509	5 2	1486 1496	43 31

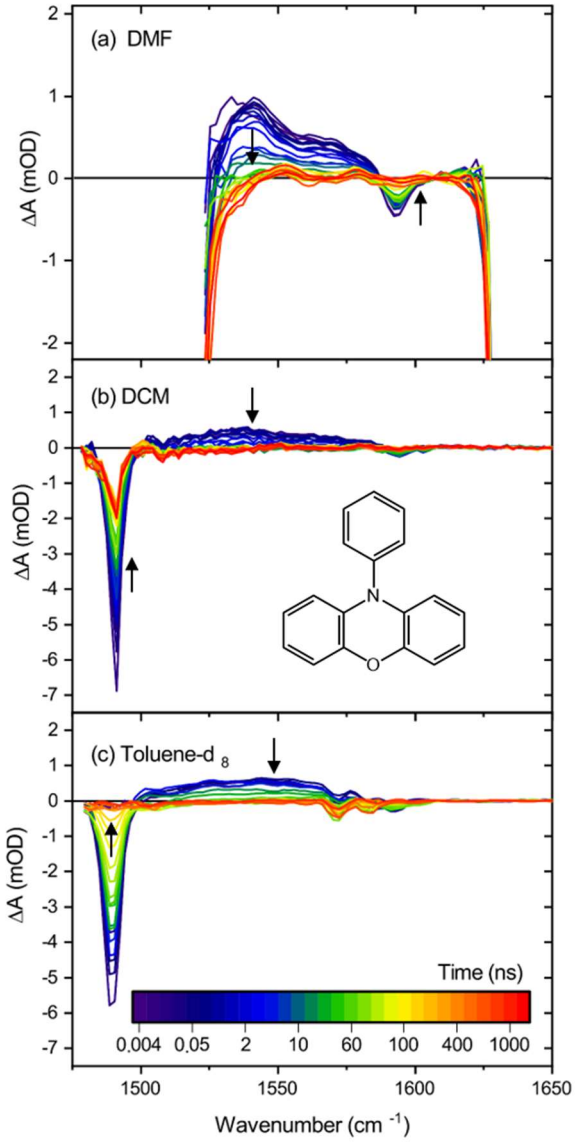

Figure 4: Transient vibrational absorption spectra obtained for the 318-nm photoexcitation of NPP in three organic solvents: (a) DMF; (b) DCM; (c) toluene-d_8 (for which the 1560 – 1590 cm^{-1} region is affected by a solvent band). The colours represent spectra obtained at different time delays after the photoexcitation, as shown by the inset key in the bottom panel. Black arrows indicate the directions of change of selected features with time. The kinetic plots obtained from analysis of these data sets are presented in Figure S9 of Supporting Information.

In toluene-d_8 the NPP GSB band centred at 1491 cm^{-1} is clearly visible and is not significantly overlapped by solvent bands or transient absorption features. It returns to the baseline within 400 ns,

indicating complete recovery of the ground-state population after photoexcitation. The time-constants for this recovery are reported in **Table 3**. The same band is evident in TVA spectra for NPP in DCM, but now the GSB recovery is only ~75% complete in 400 ns (and shows no further recovery in measurements extending to 10 μs). We attribute the incomplete ground-state recovery to excited state NPP reaction with DCM, either by electron transfer[36] or other reactive bimolecular processes. Although we see no clear evidence in TVA spectra for bands which might be assigned to $NPP^{\cdot+}$ radical cations,[14] decomposition of the TEA spectra shown in Figures S7 and S8 of Supporting Information does support this interpretation. In DMF, the observations are restricted to the aforementioned broad ESA band, which initially grows with a time constant consistent with the 14.8 ps value determined by TEAS, and a weak GSB feature centred at 1594 cm^{-1} the recovery of which is also to baseline within 400 ns. The quality of TVAS data obtained in DMF is limited by the solvent absorption and precludes direct fitting of the early time ESA band intensities. All the time constants for S_1 decay and S_0 recovery obtained from our fits are summarized in **Table 3**. The shorter NPP S_1 lifetime in DCM is consistent with the excited-state reaction with the solvent discussed above.

Table 3: Time constants obtained from bi- or tri-exponential analysis of the evolution of the intensities of bands observed by transient vibrational absorption spectroscopy and assigned to the S_0 and S_1 states of NPP. The global fitting of kinetic data for both electronic states gives matching entries in more than one column for a given solvent. The sub-picosecond time constant τ_1 observed in TEAS data (**Table 1**) was not resolved in the TVAS data and hence was not included in fits.

	S_0 [(a)]			S_1	
Solvent	τ_2 / ps (recovery)	τ_3 / ns (recovery)	τ_4 / ns (recovery)	τ_2 / ps (growth)	τ_3 / ns (decay)
DMF	–	2.1 ± 0.1	46 ± 12	– [(b)]	2.1 ± 0.1
DCM	24 ± 9	1.5 ± 0.2	43 ± 9	24 ± 9	1.5 ± 0.2
Toluene-d_8	14 ± 2	2.4 ± 0.2	27 ± 2	14 ± 2	2.4 ± 0.2

(a) Analysis of the amplitudes of the exponential fit components shows that, in all cases, the decay component with the largest time constant (τ_4) contributes most to the ground-state recovery. (b) A weak rise in the S_1 absorption band in DMF is consistent with the 14.8-ps time constant obtained from TEA data (see Table 1) but was not fitted here.

Figure 5 summarizes the observed relaxation pathways and their associated time constants, generalized to represent results from all three solvents. The S_0-state recovery time-constants τ_3 and τ_4 reported in Table 3 are assigned respectively to the relaxation from S_1 to S_0 (by fluorescence and perhaps non-radiative internal conversion), and to relaxation from T_1 to S_0 (by ISC or phosphorescence). This latter timescale suggests a relatively short-lived triplet state (T_1 lifetimes > 1 ms were reported by Sartor *et al*. [16] for N-phenyl and N-naphthyl phenoxazines with core phenyl or biphenyl substituents), which may indicate an efficient $T_1 \rightarrow S_0$ non-radiative relaxation pathway in NPP. More likely, however, is that the τ_4 values measured are a lower limit to the T_1-state lifetime because of triplet quenching by residual,

unpurged O_2 dissolved in the sample solutions or entering the sample circulation system during measurements. Indeed, test measurements made with N_2-purged solutions showed T_1 lifetimes > 1 μs, but we were unable to maintain O_2-free conditions in our circulating samples over the ~20-min durations of the experimental measurements.

The kinetic fitting also reveals sub-ns components to the S_1 band growth and GSB recovery (e.g. with time constants of τ_2 = 24 ± 9 ps in DCM and 14 ± 2 ps in toluene-d_8 which are similar to the corresponding time constants extracted from TEA spectra for S_1 population growth (Table 1). Small discrepancies in the values may reflect the effects of vibrational cooling over a few picosecond timescales in S_0. The mirroring of these time constants in the GSB recovery kinetics suggest a direct pathway to S_0 from the initially excited S_n state, or from the vibrationally excited S_1-state molecules produced promptly by the $S_n \rightarrow S_1$ internal conversion in competition with S_1 (v=0) population growth. The observed time constants of $\tau_2 \sim 20$ ps may then be determined by this IC or by vibrational cooling in the S_1 or S_0 states.

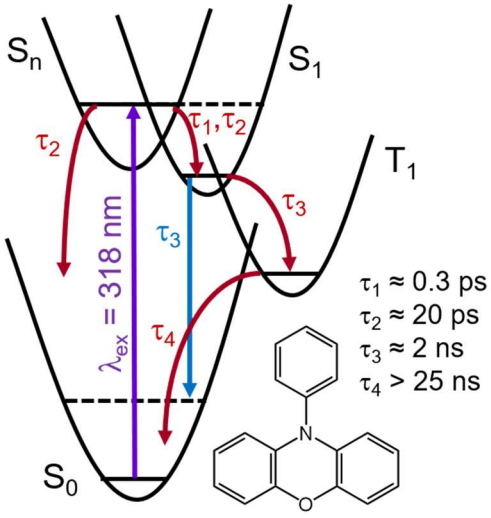

Figure 5: Schematic PE curves and relaxation pathways for the photochemistry of NPP in solution. Photoexcitation to the S_n state (n = 2 or 3) at 318 nm is followed by competitive internal conversion to S_1 and S_0 (the latter perhaps instead from vibrationally hot S_1 molecules) and vibrational energy transfer (VET) to solvent on timescales of $\tau_2 \approx 20$ ps. IC from S_n or S_1 to S_0 requires conical intersections which are not shown. The S_1 lifetime is $\tau_3 \approx 2$ ns, with decay by competing fluorescence to S_0 (blue arrow) and ISC to the triplet manifold (represented here only by the T_1 state). The T_1 state decays to S_0 on timescales $\tau_4 > 25$ ns which appear to be influenced by quenching by dissolved O_2. Horizontal solid and dashed black lines indicate the lowest and an excited vibrational level of an electronic state, respectively. The time constants specified are representative of the values found for the three solvents studied (see Tables 1 and 3).

In toluene-d_8 solution, the ratio of amplitudes of the τ_3 and τ_4 components of the tri-exponential recovery of the GSB feature observed in the TVAS measurements and attributed to S_1 and T_1 decays is 0.23 ± 0.04. With the assumption of negligible overlap of the GSB feature by ESA bands (which are weaker, as seen in Figure 4), we deduce that (81 ± 4) % of the ground-state recovery from equilibrated S_1 molecules (i.e. the S_1 population after IC from S_n and VET to the solvent) is indirectly via the T_1 state. The overall T_1 quantum yield is estimated from the amplitudes of the τ_2, τ_3 and τ_4 decay components to be $\Phi(T_1) = 0.56 \pm 0.03$. Taking the rate coefficient for loss of S_1 population to be the reciprocal of the τ_3 value from Table 3, i.e. $k(S_1) = (4.1 \pm 0.3) \times 10^8$ s^{-1}, and an ~81% branching from equilibrated S_1 into the T_1 state, we estimate an ISC rate coefficient of $k_{ISC} = (3.3 \pm 0.2) \times 10^8$ s^{-1} and a radiative lifetime for S_1 (assuming no other IC decay pathways to S_0) of ~13 ns. The k_{ISC} value derived is ~3× larger than the corresponding value measured recently for a core-substituted diphenyl NPP derivative,[16] resulting in a higher T_1 quantum yield.

The outcomes of our recent experimental studies of the photochemistry of dihydrophenazine-based OPCs in solution contrast with the current observations for the phenoxazine-based NPP. We previously reported S_1 lifetimes for selected dihydrophenazine OPCs that ranged from 0.6 – 16 ns, with considerable dependence on solvent (in experiments that also compared the photochemistry in DMF, DCM and toluene), and triplet quantum yields below 20%.[14, 19] For NPP, the S_1 state lifetimes are consistently ~2 ns irrespective of solvent choice, and in toluene (81 ± 4) % of the vibrationally equilibrated S_1-state molecules cross to the triplet manifold of states before decaying to S_0. In DMF this fraction is estimated to be 84 ± 21 %. The differences in the observed behaviour may stem from the CT vs LE character of the excited states in the two classes of OPCs. The dihydrophenazine derivatives studied have low-lying states with CT character[11] (corresponding to electron density migration from the dihydrophenazine core to the N-aryl groups) whereas the computed CT character of the S_1 and T_1 states participating in the NPP photochemistry is small (see above). Recent studies have shown that CT character can promote ISC in phenoxazine and phenothiazine OPC candidates.[13, 16] Our results for NPP and the dihydrophenazine derivatives show that other factors are also important in determining ISC quantum yields in these classes of compound. The ISC quantum yield will also be influenced by the rate of competitive non-radiative relaxation of the S_1-state population to S_0. For example, the CT-character S_1 state of 5,10-di(4-trifluoromethylphenyl)-5,10-dihydrophenazine has a sub-ns lifetime in DMF, and hence a low (< 10%) T_1 quantum yield.[14]

The energies of states with pronounced CT character are more strongly affected by the polarity of the solvent than are those with LE character. Hence, the energetic orderings and regions of crossing of S_n and T_n states ($n \geq 1$) in the dihydrophenazine compounds are more sensitive to the local environment than are those of NPP. This sensitivity will influence the use of dihydrophenazine compounds as OPCs,

but may also affect the breadth of applications of phenoxazine derivatives which are core-modified or contain N-aryl substituents such as 1-naphthyl, 2-naphthyl, or phenyl groups with electron withdrawing groups, all of which stabilize excited states with CT character.[16] Either solvent or substituent stabilization of CT states might reduce their redox potentials and perhaps also their bimolecular electron transfer rates.

Conclusions

Ultrafast transient absorption spectroscopy measurements spanning timescales from ~100 fs to 1000 ns reveal the excited state photodynamics of a model phenoxazine photoredox catalyst, N-phenyl phenoxazine after absorption of 318-nm UV radiation. Experiments conducted in three solvents, DMF, DCM and toluene examine the effects of solvent properties such as polarity on the excited state lifetimes and photochemical pathways. Transient absorption features in the UV/visible and mid-IR spectral regions are assigned with the help of electronic structure calculations of excited state energies, transition dipole moments and vibrational frequencies. The outcomes establish rapid (few-ps) internal conversion from the optically bright, photoexcited S_n state (with n = 2 or 3 dominating the excitation at the chosen UV wavelength) to the S_1 state and a ~2 ns S_1 lifetime that is largely independent of the choice of solvent. A modest shortening of the lifetime in DCM may reflect reaction with the solvent, for example by electron transfer. Recovery of ground state (S_0) NPP is complete in toluene-d_8 but occurs over three distinct timescales corresponding to relaxation from the S_n (n>1) (or vibrationally hot S_1), S_1 and T_1 states. The contributions of the three pathways indicate a quantum yield for intersystem crossing, $\Phi_{ISC} = 0.56 \pm 0.03$. The ISC pathway is also active in DMF and DCM, but incomplete ground-state recovery in DCM on a tens-of-microsecond timescale is further evidence of excited-state NPP reaction with the solvent. The high triplet quantum yield for NPP is likely to be beneficial in its application as an organic photoredox catalyst.

Acknowledgements

We gratefully acknowledge EPSRC (Grant EP/R012695/1) for funding this work. M.S is supported by a Marie Skłodowska-Curie Fellowship (MARCUS 793799). L.L.B and J.T. thank the Bristol Chemical Synthesis Centre for Doctoral Training, funded by EPSRC (EP/L015366/1), and the University of Bristol, for PhD studentships. DS acknowledges PhD studentship support from the EPSRC Theory and Modelling in Chemical Sciences Centre for Doctoral Training (EP/L015722/1). The Bristol laboratory was funded by ERC Advanced Grant CAPRI 290966. We thank Giordano Amoruso and Dr Tom Oliver (University of Bristol) for use of their time-correlated single-photon counting apparatus and help with data acquisition. The LIFEtime Facility is located at the STFC Rutherford-Appleton Laboratory, and we thank Dr Ian P. Clark for his assistance with the experimental measurements performed there.

Supporting Information

The Supporting Information contains: Details of the synthesis and characterization of N-phenyl phenoxazine samples; Steady state UV/visible, IR and fluorescence spectra of NPP in solution; Examples of decomposition of transient electronic absorption spectra; Kinetic fitting of time-dependent band intensities for transient vibrational absorption spectra; Computed structures, vibrational frequencies, and electronic transitions for NPP in its ground and excited electronic states; Computed changes in electron density for electronic transitions.

Data Availability

Data are available at the University of Bristol data repository, data.bris, at https://doi.org/10.5523/bris.d54vz8fxf0sl24lo4cy694uj3

References

1. C. K. Prier, D. A. Rankic and D. W. C. MacMillan, Visible Light Photoredox Catalysis with Transition Metal Complexes: Applications in Organic Synthesis. Chem. Rev. **113** (2013) 5322-5363.
2. C. H. Lim, M. Kudisch, B. Liu and G. M. Miyake, C-N Cross-Coupling via Photoexcitation of Nickel-Amine Complexes. J. Am. Chem. Soc. **140** (2018) 7667-7673.
3. B. J. Shields, B. Kudisch, G. D. Scholes and A. G. Doyle, Long-Lived Charge-Transfer States of Nickel(II) Aryl Halide Complexes Facilitate Bimolecular Photoinduced Electron Transfer. J. Am. Chem. Soc. **140** (2018) 3035-3039.
4. N. A. Romero and D. A. Nicewicz, Organic photoredox catalysis. Chem. Rev. **116** (2016) 10075-10166.
5. N. J. Treat, H. Sprafke, J. W. Kramer, P. G. Clark, B. E. Barton, J. R. de Alaniz, B. P. Fors and C. J. Hawker, Metal-Free Atom Transfer Radical Polymerization. J. Am. Chem. Soc. **136** (2014) 16096-16101.
6. X. C. Pan, C. Fang, M. Fantin, N. Malhotra, W. Y. So, L. A. Peteanu, A. A. Isse, A. Gennaro, P. Liu and K. Matyjaszewskit, Mechanism of Photoinduced Metal-Free Atom Transfer Radical Polymerization: Experimental and Computational Studies. J. Am. Chem. Soc. **138** (2016) 2411-2425.
7. Y. Du, R. M. Pearson, C. H. Lim, S. M. Sartor, M. D. Ryan, H. S. Yang, N. H. Damrauer and G. M. Miyake, Strongly Reducing, Visible-Light Organic Photoredox Catalysts as Sustainable Alternatives to Precious Metals. Chem. Eur. J. **23** (2017) 10962-10968.
8. R. M. Pearson, C. H. Lim, B. G. McCarthy, C. B. Musgrave and G. M. Miyake, Organocatalyzed Atom Transfer Radical Polymerization Using N-Aryl Phenoxazines as Photoredox Catalysts. J. Am. Chem. Soc. **138** (2016) 11399-11407.
9. J. C. Theriot, C. H. Lim, H. Yang, M. D. Ryan, C. B. Musgrave and G. M. Miyake, Organocatalyzed atom transfer radical polymerization driven by visible light. Science **352** (2016) 1082-1086.
10. S. Jockusch and Y. Yagci, The active role of excited states of phenothiazines in photoinduced metal free atom transfer radical polymerization: singlet or triplet excited states? Polym. Chemi. **7** (2016) 6039-6043.
11. C. H. Lim, M. D. Ryan, B. G. McCarthy, J. C. Theriot, S. M. Sartor, N. H. Damrauer, C. B. Musgrave and G. M. Miyake, Intramolecular charge transfer and ion pairing in N,N-diaryl dihydrophenazine photoredox catalysts for efficient organocatalyzed atom transfer radical polymerization. J. Am. Chem. Soc. **139** (2017) 348-355.

12. B. G. McCarthy, R. M. Pearson, C. H. Lim, S. M. Sartor, N. H. Damrauer and G. M. Miyake, Structure-Property Relationships for Tailoring Phenoxazines as Reducing Photoredox Catalysts. J. Am. Chem. Soc. **140** (2018) 5088-5101.
13. S. M. Sartor, B. G. McCarthy, R. M. Pearson, G. M. Miyake and N. H. Damrauer, Exploiting Charge-Transfer States for Maximizing Intersystem Crossing Yields in Organic Photoredox Catalysts. J. Am. Chem. Soc. **140** (2018) 4778-4781.
14. D. Koyama, H. J. A. Dale and A. J. Orr-Ewing, Ultrafast dynamics of a bimolecular organocatalysed photoredox reaction. J. Am. Chem. Soc. **140** (2018) 1285-1293.
15. A. J. Orr-Ewing, How can ultrafast laser spectroscopy inform the design of new organic photoredox catalysts for chemical and materials synthesis? . Structural Dynamics **6** (2019) 010901.
16. S. M. Sartor, Y. M. Lattke, B. G. McCarthy, G. M. Miyake and N. H. Damrauer, Effects of Naphthyl Connectivity on the Photophysics of Compact Organic Charge-Transfer Photoredox Catalysts. J. Phys. Chem. A **123** (2019) 4727-4736.
17. S. M. Sartor, C. H. Chrisman, R. M. Pearson, G. M. Miyake and N. H. Damrauer, Designing high triplet yield phenothiazine donor-acceptor complexes for photoredox catalysis. J. Phys. Chem. A **124** (2020) 817-823.
18. A. Bhattacherjee, M. Sneha, L. Lewis-Borrell, O. Tau, I. P. Clark and A. J. Orr-Ewing, Picosecond to millisecond tracking of a photocatalytic decarboxylation reaction provides direct mechanistic insights. Nat. Commun. **10** (2019) 5152.
19. L. Lewis-Borrell, M. Sneha, A. Bhattacherjee, I. P. Clark and A. J. Orr-Ewing, Mapping the multi-step mechanism of a photoredox catalyzed atom-transfer radical polymerization reaction by direct observation of the reactive intermediates Chem. Sci. (submitted) (2020).
20. N. A. Romero and D. A. Nicewicz, Mechanistic Insight into the Photoredox Catalysis of Anti-Markovnikov Alkene Hydrofunctionalization Reactions. J. Am. Chem. Soc. **136** (2014) 17024-17035.
21. S. Ruccolo, Y. Qin, C. Schnedermann and D. G. Nocera, General Strategy for Improving the Quantum Efficiency of Photoredox Hydroamination Catalysis. J. Am. Chem. Soc. **140** (2018) 14926-14937.
22. A. Rosspeintner, B. Lang and E. Vauthey, Ultrafast Photochemistry in Liquids. Annu Rev Phys Chem **64** (2013) 247-271.
23. T. Kumpulainen, B. Lang, A. Rosspeintner and E. Vauthey, Ultrafast Elementary Photochemical Processes of Organic Molecules in Liquid Solution. Chem. Rev. **117** (2017) 10826-10939.
24. R. K. Venkatraman, S. Kayal, A. Barak, A. J. Orr-Ewing and S. Umapathy, Intermolecular hydrogen bonding controlled intersystem crossing rates of benzophenone. J. Phys. Chem. Lett. **9** (2018) 1642-1648.
25. R. K. Venkatraman and A. J. Orr-Ewing, Photochemistry of Benzophenone in Solution: A Tale of Two Different Solvent Environments. J. Am. Chem. Soc. **141** (2019) 15222-15229.
26. G. M. Roberts, H. J. B. Marroux, M. P. Grubb, M. N. R. Ashfold and A. J. Orr-Ewing, On the Participation of Photoinduced N-H Bond Fission in Aqueous Adenine at 266 and 220 nm: A Combined Ultrafast Transient Electronic and Vibrational Absorption Spectroscopy Study. J. Phys. Chem. A **118** (2014) 11211-11225.
27. K. Röttger, H. J. B. Marroux, A. F. M. Chemin, E. Elsdon, T. A. A. Oliver, S. T. G. Street, A. S. Henderson, M. C. Galan, A. J. Orr-Ewing and G. M. Roberts, Is UV-induced electron-driven proton transfer active in a chemically modified A-T DNA base pair? J. Phys. Chem. B **121** (2017) 4448-4455.
28. G. M. Greetham, P. M. Donaldson, C. Nation, I. V. Sazanovich, I. P. Clark, D. J. Shaw, A. W. Parker and M. Towrie, A 100 kHz Time-Resolved Multiple-Probe Femtosecond to Second Infrared Absorption Spectrometer. Appl. Spectrosc. **70** (2016) 645-653.
29. D. Koyama, P. M. Donaldson and A. J. Orr-Ewing, Femtosecond to microsecond observation of the photochemical reaction of 1,2-di(quinolin-2-yl)disulphide with methyl methacrylate. Phys. Chem. Chem. Phys. **19** (2017) 12981-12991.
30. M. P. Grubb, A. J. Orr-Ewing and M. N. R. Ashfold, KOALA: A program for the processing and decomposition of transient spectra. Rev. Sci. Instrumen. **85** (2014) 064104.
31. M. J. Frisch, G. W. Trucks, H. B. Schlegel, G. E. Scuseria, M. A. Robb, J. R. Cheeseman, G. Scalmani, V. Barone, B. Mennucci, G. A. Petersson, H. Nakatsuji, M. Caricato, X. Li, H. P. Hratchian, A. F. Izmaylov, J. Bloino, G. Zheng, J. L. Sonnenberg, M. Hada, M. Ehara, K. Toyota, R. Fukuda, J.

Hasegawa, M. Ishida, T. Nakajima, Y. Honda, O. Kitao, H. Nakai, T. Vreven, J. A. Montgomery, J. E. Peralta, F. Ogliaro, M. J. Bearpark, J. J. Heyd, E. Brothers, K. N. Kudin, V. N. Staroverov, R. Kobayashi, J. Normand, K. Raghavachari, A. Rendell, J. C. Burant, S. S. Iyengar, J. Tomasi, M. Cossi, N. Rega, J. M. Millam, M. Klene, J. E. Knox, J. B. Cross, V. Bakken, C. Adamo, J. Jaramillo, R. Gomperts, R. E. Stratmann, O. Yazyev, A. J. Austin, R. Cammi, C. Pomelli, J. W. Ochterski, R. L. Martin, K. Morokuma, V. G. Zakrzewski, G. A. Voth, P. Salvador, J. J. Dannenberg, S. Dapprich, A. D. Daniels, O. Farkas, J. B. Foresman, J. V. Ortiz, J. Cioslowski and D. J. Fox *Gaussian 09*, Gaussian Inc., Wallingford CT, 2009.

32. D. O. Kashinski, G. M. Chase, R. G. Nelson, O. E. Di Nallo, A. N. Scales, D. L. VanderLey and E. F. C. Byrd, Harmonic Vibrational Frequencies: Approximate Global Scaling Factors for TPSS, M06, and M11 Functional Families Using Several Common Basis Sets. J Phys Chem A **121** (2017) 2265-2273.

33. F. Neese, The ORCA program system. Wires Comput Mol Sci **2** (2012) 73-78.

34. T. Lu and F. W. Chen, Multiwfn: A multifunctional wavefunction analyzer. J Comput Chem **33** (2012) 580-592.

35. K. Röttger, H. J. B. Marroux, H. Bohnke, D. T. J. Morris, A. T. Voice, F. Temps, G. M. Roberts and A. J. Orr-Ewing, Probing the excited state relaxation dynamics of pyrimidine nucleosides in chloroform solution. Faraday Discuss **194** (2016) 683-708.

36. S. Chaudhuri, B. Rudshteyn, M. Premont-Schwarz, D. Pines, E. Pines, D. Huppert, E. T. J. Nibbering and V. S. Batista, Ultrafast photo-induced charge transfer of 1-naphthol and 2-naphthol to halocarbon solvents. Chem Phys Lett **683** (2017) 49-56.